International Journal of Nanomedicine

Dovepress
Taylor & Francis Group

Open Access Full Text Article

ORIGINAL RESEARCH

Therapeutic Potential of PDA@CeO2 in Suppressing Hepatic Stellate Cell Activation and Preventing Liver Fibrosis

Han-mei Li[1],*, Ju-ying Zhang[1],*, Xiao-qing Wang[1], Li-tao Ye[1], Bo Ren[1], Yi-han Leng[1], Ji-xuan Zhang[2], You Yang[1], Qiong Jiang[1], Lin-li Feng[1], Yang Li[2], Jin-hong Yu[1]

[1]Department of Ultrasound, Affiliated Hospital of North Sichuan Medical College, Innovation Centre for Science and Technology of North Sichuan Medical College, Nanchong, Sichuan, 637000, People's Republic of China; [2]Department of Radiology, Affiliated Hospital of North Sichuan Medical College, Nanchong, Sichuan, People's Republic of China

*These authors contributed equally to this work

Correspondence: Jin-hong Yu; Yang Li, Email yujinhong@nsmc.edu.cn; 552410618@qq.com

Objective: Liver fibrosis replaces healthy tissue with scar tissue, potentially leading to cirrhosis and cancer. ROS drive this process by activating hepatic stellate cells. This study tests the hepatoprotective effects of PDA@CeO_2 nanoparticles in scavenging ROS, inhibiting HSC activation, and delaying fibrosis, using 2D-SWE to assess treatment efficacy.

Methods: In vitro, flow cytometry evaluated ROS levels in HSCs, scratch assays assessed migration, and α-SMA expression confirmed activation. In vivo, PDA@CeO_2 NPs were tested in rats with CCl4-induced liver fibrosis, with effects monitored by 2D-SWE. Histopathological staining and fibrosis markers (Collagen I, α-SMA, TGF-β/Smad3, NOX4) assessed fibrosis progression.

Results: In vitro, PDA@CeO_2 reduced ROS levels and inhibited HSC migration, with decreased α-SMA expression indicating suppressed activation. In vivo, PDA@CeO_2 treatment in CCl4-induced liver fibrosis rats reduced fibrosis markers. 2D-SWE showed improved liver stiffness, and histopathological analysis revealed reduced fibrosis and inflammation. The therapeutic effects were linked to modulation of the NOX4-TGF-β/Smad3 pathway, attenuating fibrosis progression.

Conclusion: This study demonstrates the potential of PDA@CeO_2 NPs as a novel treatment for liver fibrosis. These nanoparticles scavenge ROS and modulate inflammatory pathways, targeting key signaling mechanisms like the NOX4-TGF-β/Smad3 pathway. PDA@CeO_2 NPs offer a promising strategy for attenuating fibrosis at cellular and molecular levels. Additionally, 2D-SWE provides a non-invasive tool for monitoring therapeutic outcomes, positioning PDA@CeO_2 NPs as a promising candidate for future clinical liver fibrosis treatments.

Keywords: PDA@CeO_2, hepatic fibrosis, 2D-SWE, hepatic stellate cells

Introduction

Liver fibrosis presents a critical and pressing health issue. It has various causes and typically progresses over time.[1] As the condition advances, it often leads to cirrhosis and may eventually result in hepatocellular carcinoma and liver failure.[2,3] In the early stages, sustained hepatocellular injury leads to excessive ROS production, which disrupts the homeostasis of the liver's microenvironment.[4,5] HSC play roles such as storing fat-soluble substances (eg, vitamin A) while maintaining the hepatic microenvironment in a quiet state.[6,7] Following liver injury, in response to ROS, quiescent hepatic stellate cells are activated by oxidative stress, promoting inflammation and extracellular matrix deposition.[8,9] This process is regulated by TGF-β-induced Smad phosphorylation and ROS signaling, both of which synergistically promote the production of extracellular matrix (ECM), including the synthesis of collagen and α-SMA, ultimately leading to liver fibrosis.[10] NOX4 is crucial in the ROS signaling pathway, particularly in the development of liver fibrosis.[11] Upon liver injury, NOX4 expression is upregulated in HSCs, leading to increased ROS

Received: 27 February 2025
Accepted: 9 July 2025
Published: 15 July 2025

production.[12] These ROS activate signaling pathways, including TGF-β/Smad, which promote the synthesis of ECM components such as collagen and α-SMA, contributing to fibrosis.[13–16] Inhibiting NOX4-mediated ROS production can mitigate HSC activation, reduce ECM deposition, alleviate inflammation, and promote liver regeneration, making it a promising therapeutic strategy for preventing or treating liver fibrosis and other ROS-related disorders. Currently, there are no drugs approved for clinical use in the treatment of liver fibrosis.[17] Considering the critical role of reactive oxygen species (ROS) in liver fibrosis, targeting oxidative stress has been proposed as a potential therapeutic strategy.[18–20]

Therefore, investigating antioxidant treatments to alleviate oxidative stress and inhibit the progression of fibrosis holds significant clinical relevance. Ceria-based nanozymes (CeO_2) have garnered attention for their ability to scavenge ROS and protect against conditions like atherosclerosis,[21] rheumatoid arthritis,[22] and hepatitis.[23–25] Due to their strong redox potential, CeO_2 NPs show therapeutic promise for liver diseases, mitigating liver injuries caused by substances like diethylnitrosamine,[26] acetaminophen,[27] and doxorubicin.[28] In non-alcoholic fatty liver disease (NAFLD), CeO_2 NPs reduce markers of liver damage, including steatosis, and inflammation.[29] However, CeO_2 NPs tend to agglomerate and are challenging to degrade, limiting their practical applications.[30] In contrast, polydopamine (PDA) NPs are biodegradable and biocompatible, offering excellent radical-scavenging properties.[31,32] PDA is a polymer that mimics the adhesive properties of mussel foot proteins, which allows it to adhere strongly to various surfaces. It is synthesized through the oxidation of dopamine, a naturally occurring catecholamine, and can form stable, thin coatings on a wide range of materials. Due to its biocompatibility, biodegradability, and strong adhesion capabilities, PDA has been explored for a variety of biomedical applications, including drug delivery, wound healing, and tissue engineering.[33,34] Furthermore, PDA NPs have been shown to protect against liver injury and treat inflammation. When combined with metals such as CeO_2, the hybrid PDA@CeO_2 nanocomposites, which combine the antioxidative properties of CeO_2 with the biocompatibility of PDA, exhibit superior ROS scavenging activity, making them a promising strategy for treating liver fibrosis.[35,36]

The early diagnostic research on liver fibrosis is limited by the lack of highly accurate and non-invasive methods, with current techniques often unable to detect fibrosis at its initial stages effectively. During the course of the study, 2D-SWE provided non-invasive, real-time measurements of hepatic stiffness that correlated directly with the severity of fibrosis. 2D-SWE is a type of ultrasound elastography that measures the stiffness of tissues by generating shear waves within the liver and detecting the speed at which these waves propagate. The faster the shear waves travel, the stiffer the tissue, which correlates with the degree of fibrosis. This method offers a detailed, two-dimensional map of the liver's stiffness, allowing for precise localization of regions with different levels of stiffness.[37–39] The advantages of 2D-SWE include its ability to evaluate the entire liver in real time, providing a comprehensive assessment of hepatic stiffness. It is non-invasive, relatively inexpensive, and does not require contrast agents, making it suitable for repeated use in monitoring disease progression. Furthermore, the ability to capture regional stiffness variations enhances diagnostic accuracy, providing a more detailed understanding of the liver's condition compared to traditional imaging techniques. This technology not only improves diagnostic precision but also supports the monitoring of disease progression over time.

Based on the significant therapeutic potential of PDA@CeO_2 NPs, this study introduces an innovative approach by integrating 2D-SWE with PDA@CeO_2 NPs to assess liver fibrosis models and their therapeutic effects. While related research has explored these technologies individually, the combination of 2D-SWE and PDA@CeO2 NPs for the diagnosis and treatment of early-stage liver fibrosis is proposed for the first time. This innovative integration provides new perspectives and methodologies for the early detection and management of liver fibrosis. By using 2D-SWE technology to evaluate the impact of PDA@CeO_2 on early-stage liver fibrosis, this study demonstrates a groundbreaking application of this technology in liver disease treatment, advancing both diagnostic and therapeutic strategies. The method not only enables precise assessment of liver stiffness and fibrosis progression but also facilitates real-time monitoring of treatment efficacy, offering valuable scientific, clinical, and technological insights for future clinical implementation and technological innovation.

Materials and Methods

Ammonium hydroxide (AR, 25–28%), nitrate hexahydrate ($Ce(NO_3)_3.6H_2O$), and dopamine (DA) were from Macklin Biochemical Technology Co. Ltd (Shanghai, China). DPPH and ABTS were purchased from Leagene Biotechnology Co., Ltd. (Beijing, China). CCK-8 assay was purchased from Bea Biotechnology Co. 4′,6-Diamino-2-phenylindole (DAPI) was purchased from Solar Biotech (Beijing, China). iFluor^{TM} 594 Conjugated Goat anti-rabbit IgG, α-SMA Monoclonal Antibody, and GAPDH were purchased from HuaAn Biotechnology Co., Ltd. (Hangzhou, China). TGF-β1 was purchased from Abbkine Scientific Co., Ltd. (Wuhan, China). HUVEC cells were obtained from the Science and Technology Innovation Center of Chuanbei Medical College. HSC-T6 cells were purchased from Priscilla Biotechnology (Wuhan, China).

Preparation of CeO_2-NPs

Cerium oxide NPs were synthesized using a chemical precipitation method.[40] First, 50 mL of anhydrous ethanol was mixed with 5 mmol of cerium(III) nitrate hexahydrate and stirred vigorously for approximately 10 minutes. Then, 20 mL of ammonium hydroxide was slowly added, and the mixture was stirred continuously overnight. The nanoparticles were collected by centrifugation, then rinsed with anhydrous ethanol and deionized water through repeated centrifugation. A yellow precipitate was obtained after vacuum freeze-drying overnight.

Preparation of PDA-NPs

45 milligrams of dopamine hydrochloride were dissolved in 25 mL of purified water. Sodium hydroxide was added while stirring to adjust the pH to approximately 9. The solution was then stirred continuously for 2 hours at room temperature. Afterward, the black PDA NPs were collected by centrifugation and thoroughly rinsed with deionized water. Finally, the nanoparticles were freeze-dried under vacuum.

Preparation of PDA@CeO_2 NPs

The PDA NPs synthesized in the previous steps were collected. Cerium nitrate hexahydrate was then added to the PDA solution, allowing Ce^{3+} ions to bind to the catechol groups of PDA. In the alkaline environment generated by ammonium hydroxide, the Ce^{3+} ions were oxidized to cerium oxide, which coated the surface of the PDA. Finally, the samples were separated by centrifugation and repeatedly rinsed with deionized water to yield PDA@CeO_2 NPs.

Characterization

The synthesized CeO_2, PDA, and PDA@CeO_2 NPs were dispersed in ultrapure water, followed by particle size analysis with a laser diffraction instrument and zeta potential measurement with a zeta potential analyzer. The morphology of CeO_2, PDA, and PDA@CeO_2 NPs were characterized using transmission electron microscopy.

Stability Evaluation of PDA@CeO_2 NPs

The stability of PDA@CeO_2 NPs was assessed by measuring their zeta potential and particle size over a 7-day period. Measurements were performed at the following time points: 0.5, 1, 2, 3, 4, 5, 6, and 7 days. At each time point, the zeta potential and particle size were measured three times to ensure consistency and reliability of the results.

Scavenging of DPPH and ABTS

The radical scavenging activities of CeO_2, PDA, and PDA@CeO_2 NPs were evaluated using the DPPH and ABTS assays. DPPH and ABTS solutions were prepared by dissolving them in ethanol, and these solutions were mixed with aqueous solutions of CeO_2, PDA, and PDA@CeO_2 NPs at varying concentrations. In addition, ascorbic acid (VC) was included as a positive control, and its concentration was adjusted to match that of the nanoparticle solutions for comparison. The mixtures were incubated at 37°C for 1 hour under light protection to ensure proper reaction conditions. After incubation, the samples were centrifuged, and the supernatant was collected for further analysis. The absorbance of

DPPH and ABTS was measured at 517 nm and 734 nm, respectively, using a UV-Vis spectrophotometer. The radical scavenging activity was calculated by determining the clearance (percentage inhibition) using the appropriate formulas.

Cell Culture and Model Establishment

In this study, HSC-T6 cells, which are rat hepatic stellate cells, were grown in DMEM medium containing 10% fetal bovine serum and placed in a 37°C incubator with 5% carbon dioxide for incubation. To activate the HSC-T6 cells, 5 ng/mL of TGF-β1 was added to DMEM containing 1% fetal bovine serum.

Cell Biocompatibility

The biocompatibility of CeO_2, PDA, and PDA@CeO_2 on HSC-T6 cells and HUVEC was evaluated with the CCK-8 assay. The procedure was as follows: Cells were seeded in 96-well plates at a density of 8000–10,000 cells per well and incubated with different concentrations of CeO_2, PDA, or PDA@CeO_2 solutions for 8 hours, respectively. Excess material was then removed by washing with PBS buffer. Next, 10 µL of CCK-8 solution was added to each well and incubated for 30 minutes to 1 hour in the dark. The absorbance at 450 nm was then measured using a UV spectrophotometer, and cell viability was calculated using the appropriate formula.

Intracellular ROS Scavenging Measurement

Intracellular ROS levels were measured using DCFH-DA. The procedure was as follows: cells were divided into several groups: a control group, a TGF-β1 activation group (5 ng/mL for 12 hours), and groups treated overnight with different concentrations of CeO_2, PDA, or PDA@CeO_2 (200 µg/mL) following activation. The medium was then replaced with a fresh staining solution containing DCFDA for the total ROS assay. After PBS washing, images were taken with a fluorescence microscope, and the intracellular ROS levels were also analyzed by flow cytometry. The fluorescence intensity of the cells was subsequently measured and quantified using ImageJ software.

Alleviation of Oxidative Stress to Avoid HSC Activation

Elevated oxidative stress is strongly linked to the progression of liver fibrosis. Reducing oxidative stress to prevent the activation of stellate cells may provide an effective strategy for managing liver fibrosis. In addition, the activation status of HSCs was verified by immunofluorescence staining. Specifically, TGF-β1-activated HSC-T6 cells were treated with PDA@CeO_2, PDA, and CeO_2 in different groups. The cells were initially fixed with 4% methanol for 10 minutes, followed by blocking with BSA for 1 hour. Subsequently, the cells were incubated with the primary antibody α-SMA (dilution 1:500) overnight at 4°C. After washing, the secondary antibody (iFluor^{TM} 594 Conjugated Goat anti-rabbit IgG) was added and incubated for 1 hour. Nuclei were stained with DAPI for 10 minutes, and the images were captured using a fluorescent microscope. The expression of α-SMA was quantified by analyzing the fluorescence intensity, which reflects the degree of HSC activation under different treatments.

Wound-Healing Assay

HSC-T6 cells were seeded in 6-well plates at a density of approximately 8×10^4 cells per well. Once the cells had adhered and formed a thin monolayer, they were scratched using the tip of a sterile pipette. The cells were then rinsed with PBS to remove any excess cell debris. In addition to the control group, HSC-T6 cells were exposed to 5 ng/mL TGF-β1 for 24 hours, followed by treatment with CeO_2, PDA, and PDA@CeO_2 (200 µg/mL), respectively. Wound images were captured using an inverted microscope at 0 and 24 hours. The relative cell migration rates were calculated using the formula: (W(0h) - W(24h)) / W(0h)%.

Transwell Assay

To evaluate the impact of different treatments on cell migration, a Transwell assay was conducted. Cells were seeded into the upper chamber of the Transwell inserts at a density of approximately 1×10^5 cells per well. The lower chamber contained medium supplemented with 10% fetal bovine serum (FBS), and the experimental groups included treatments with TGF-β1, or TGF-β1 combined with CeO_2, PDA, and PDA@CeO_2. The control group received only the culture medium. After a 24-hour incubation period to allow cell migration, the cells that migrated to the lower surface of the membrane were fixed with formaldehyde and stained with crystal violet. Migrated cells were then observed and quantified under a microscope, with five random fields selected for counting in each well. The average number of migrated cells was calculated for each experimental group. This method provides a reliable approach for assessing the effects of different treatments on cell migration.

Cellular Uptake Efficiency of PDA@CeO_2 NPs in Hepatocytes, Activated HSC-T6, and HSC-T6 Cells

The cellular uptake efficiency of DiI-labeled PDA@CeO_2 NPs was evaluated by comparing hepatocytes, activated HSC-T6 cells (treated with 5 ng/mL TGF-β1 for 12 hours), and HSC-T6 cells. Different cell types were incubated with DiI-labeled PDA@CeO_2 NPs for 6 hours. After incubation, the cells were fixed and stained with DAPI to label the nuclei. Cellular uptake was then observed using confocal laser scanning microscopy. To further validate the differences in nanoparticle uptake among the cell types, flow cytometry was performed on cells incubated with DiI-labeled PDA@CeO_2 NPs for 6 hours, allowing for quantitative assessment of the uptake efficiency across the different cell types.

Animal

The experimental animals were kept in plastic cages and given a regular diet and water in a pathogen-free environment. The environmental conditions were maintained at a temperature of 24 ± 1°C, a relative humidity of 55 ± 5%, and a 12-hour light/dark cycle. All animal studies received approval from the Animal Research Committee of North Sichuan Medical College (protocol [2024028]) and were conducted in compliance with the Guide for the Care and Use of Laboratory Animals.

The experimental groups included a control group, liver fibrosis model group, and different treatment groups of the liver fibrosis model (CeO_2, PDA, PDA@CeO_2). In the control group, rats were given subcutaneous injections of olive oil twice a week. For the liver fibrosis model animals, a solution of carbon tetrachloride and olive oil mixed in a 2:3 ratio was administered subcutaneously twice a week at a dose of 1 mL/kg for 8 weeks. In the different treatment groups, after 4 weeks of carbon tetrachloride injection, depending on the subgroup, rats received weekly tail vein injections of CeO_2, PDA, or PDA@CeO_2 twice a week during the modeling period.

Safety Evaluation

The body weight of all experimental rats was recorded weekly. At the end of the treatment, blood samples were collected for liver and kidney function tests, and the animals were euthanized. Liver photographs were taken to assess the therapeutic effects. To evaluate the biosafety of CeO_2, PDA, and PDA@CeO_2, euthanasia was performed on the rats at the end of the treatment. The heart, liver, spleen, lungs, and kidneys of each animal were then collected and fixed in formaldehyde for hematoxylin and eosin (HE) staining.

Hemolysis Assay

A hemolysis assay was conducted to evaluate the hemocompatibility of CeO_2, PDA, and PDA@CeO_2. Blood was collected from SD rats into heparinized tubes, and after centrifugation at 5000 rpm for 15 minutes, the erythrocyte pellet was collected, discarding the supernatant. The erythrocytes were then resuspended in PBS buffer. A total of 1.5 mL of the erythrocyte suspension was mixed with different concentrations of CeO_2, PDA, and PDA@CeO_2 solutions and incubated for 1 hour. Following centrifugation at 5000 rpm for 15 minutes, 100 μL of the supernatant was obtained, and its absorbance was recorded at 540 nm using an enzyme-linked instrument.

Biological Distribution of PDA@CeO_2 NPs

This study employed a liver fibrosis rat model to investigate the in vivo biodistribution of IR-820-labeled PDA@CeO_2 NPs at various time points (4h, 8h, 12h, 24h, 48h, 72h) following intravenous injection. After injection, fluorescence imaging was performed using an in vivo imaging system (IVIS), with appropriate excitation and emission wavelengths set to detect the fluorescence signals. The biodistribution of the nanoparticles in major organs such as the heart, liver, spleen, lungs, and kidneys was observed and analyzed.

Histopathological Evaluation of Therapeutic Effects

Liver tissues from different groups (Control, Modal, CeO_2, PDA, and PDA@CeO_2) were fixed in paraformaldehyde, processed for paraffin embedding, and sectioned for subsequent staining. The sections were stained with H&E, Sirius red, α-SMA immunohistochemistry, and Masson's staining. Liver fibrosis was semi-quantified by evaluating fibrous deposition observed in Sirius red staining, while the extent of collagen accumulation was further quantified through Masson staining. Additionally, α-SMA expression was assessed to evaluate the activation of hepatic stellate cells. All quantifications were performed using image analysis software.

Ultrasound Measurements of Parameters

Ultrasound elastography was performed at weeks 0, 4, 6, and 8 to assess liver stiffness in different groups (Control, Model, CeO_2, PDA, and PDA@CeO_2). The procedure was conducted using a Resona R9 ultrasound scanner (Mindray, China) with a linear array probe (L14-3W) operating within a frequency range of 6.0–15.4 MHz. Prior to imaging, rats were anesthetized with isoflurane inhalation. After securing the rat in a fixed position, the fur in the examination area was shaved. A real-time 2D liver image was obtained, and a 5 mm × 5 mm region of interest (ROI) was selected in the liver parenchyma (1.0 cm below the capsule), avoiding large blood vessels and bile ducts. Measurements of the maximum (Emax), mean (Emean), and minimum (Emin) values of Young's modulus were recorded, with each value being repeated five times. Image quality was considered successful if the respiratory motion index was ≥ 4 green stars and the confidence index was ≥ 95%.

Western Blotting

Protein was extracted from liver tissue by adding a phosphatase inhibitor, followed by homogenization using an ultrasonic crusher and boiling at 100°C for 10 minutes. The samples were then subjected to electrophoresis on SDS-PAGE gels and transferred onto PVDF membranes. The protein concentration for loading was 20 μg/μL, and the sample volume used was 6 μL. The membranes were incubated with 5% skimmed milk for 1 hour to block nonspecific binding. Subsequently, primary antibodies (monoclonal antibodies against type I collagen, α-SMA, TGF-β1, Smad3, P-Smad3, and NOX4) were applied and incubated for 12–16 hours at 4°C. The dilution of the primary antibodies was prepared according to the product instructions, typically at a dilution of 1/1000 to 1/10000. Following three washes of the membranes with TBST, they were incubated with the secondary antibody for 1.5 hours at room temperature. Following washing, a developing solution was applied, and the membranes were imaged using a gel visualizer. The relative expression levels of each target protein were assessed by calculating the grayscale ratio of the target protein bands to GAPDH.

Statistical Analysis

Statistical analyses were conducted using GraphPad Prism 8 software. Data that followed a normal distribution are presented as mean ± standard deviation (x ± s). An unpaired *t*-test was used to compare two groups, while one-way or multifactorial ANOVA was applied for comparisons among multiple groups. A P-value less than 0.05 was regarded as statistically significant. The thresholds for statistical significance were set as follows: *$P < 0.05$, **$P < 0.01$, ***$P < 0.001$, and ****$P < 0.0001$, with "ns" denoting no significant difference.

Results

Nanodrug Synthesis and Characterization

The schematic of PDA@CeO_2 NPs synthesis is shown in Figure 1A. PDA NPs were initially formed through the self-polymerization of dopamine (DA) under alkaline conditions. Subsequently, cerium oxide coating was applied by adding cerium nitrate hexahydrate to the PDA solution. Transmission electron microscopy (TEM) images revealed that the

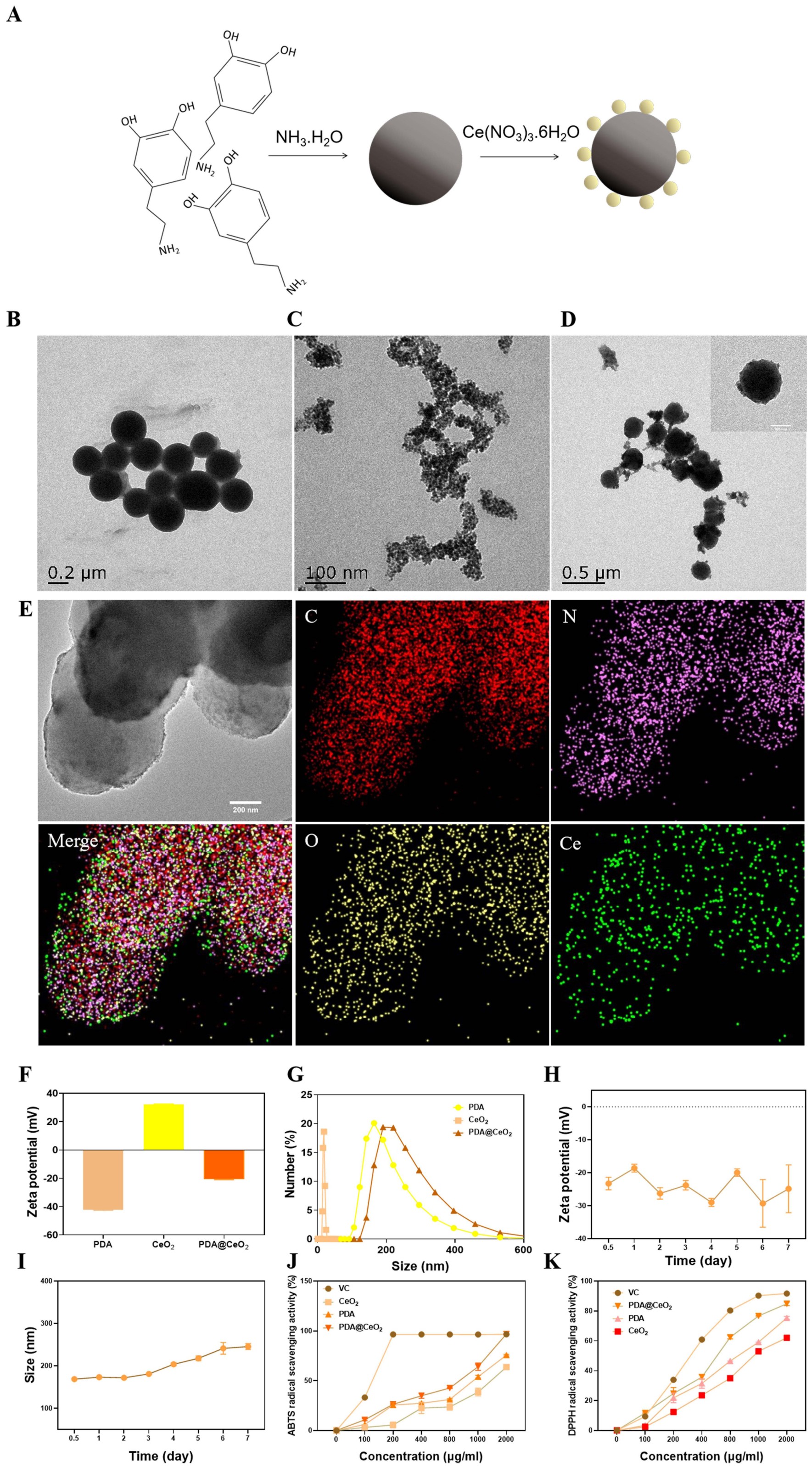

Figure 1 (**A**) Schematic diagram of synthesis of PDA@CeO_2 NPs. (**B**–**D**) TEM image of CeO_2 NPs, PDA NPs and PDA@CeO_2 NPs. Inset: TEM image of a single nanoparticle, scale bar: 100 nm. (**E**) TEM image and corresponding EDX elemental mapping (C, N, O and Ce elements) of the PDA@CeO_2 NPs. (**F**) Zeta potential change of PDA NPs, CeO_2 NPs and PDA@CeO_2 NPs. (**G**) Particle size distribution of PDA NPs, CeO_2 NPs and PDA@CeO_2 NPs. (**H**) Zeta potential values of PDA@CeO_2 measured continuously over 7 days. Data are presented as the mean ± standard deviation (n=3). (**I**) Particle size variation of PDA@CeO_2 measured continuously over 7 days. Data are presented as the mean ± standard deviation (n=3). (**J**) Line graph showing the ABST clearance efficiency of different groups: VC group, PDA NPs, CeO_2 NPs, and PDA@CeO_2 NPs. Data are presented as the mean ± standard deviation (n=3). (**K**) DPPH clearance efficiency for different groups (VC group, PDA NPs, CeO_2 NPs, and PDA@CeO_2 NPs). Data are expressed as the mean ± standard deviation (n=3).

surface of the PDA NPs was smooth (Figure 1B). CeO_2 NPs exhibit more pronounced agglomeration (Figure 1C). As shown in Figure 1D, the surface of the PDA NPs became roughened after being coated with CeO_2 NPs. The results of EDX elemental mapping analysis of the PDA@CeO_2 NPs revealed a more homogeneous spread of C, N, O, and Ce (Figure 1E). Zeta potential analysis showed that the potentials of PDA NPs, CeO_2 NPs, and PDA@CeO_2 NPs were −42.17 ± 0.45 mV, 31.97 ± 0.51 mV, and −20.77 ± 0.25 mV, respectively (Figure 1F). The average particle size of individual CeO_2 NPs was 14.4 ± 1.9 nm. In contrast, the hydrodynamic diameter of PDA@CeO_2 was slightly larger than that of PDA NPs, measuring 168.76 ± 6.28 nm (Figure 1G). As shown in Figure 1H and I, the zeta potential and particle size were continuously monitored over a period of 7 days, indicating good stability. The UV-vis spectrum of the PDA@CeO_2 NPs displayed a distinctive absorption peak at 296 nm, which was attributed to cerium oxide, confirming that CeO_2 NPs were successfully encapsulated on the PDA NPs (Figure SI 1A).

ROS Scavenging Activity

The PDA@CeO_2 composite demonstrated superior radical scavenging activity compared to the individual PDA and CeO_2, as shown in Figure 1J and K. Specifically, the PDA@CeO_2 hybrid exhibited enhanced ABTS and DPPH radical scavenging capacities, owing to the combined effect of PDA and CeO_2. While PDA alone showed moderate radical scavenging activity and CeO_2 exhibited a limited effect, the combination of PDA and CeO_2 significantly improved the overall scavenging efficiency. This enhancement is likely due to the increased surface area and the interaction between the functional groups on PDA and the CeO_2 NPs, which facilitates more effective scavenging of both ABTS and DPPH radicals. However, despite the enhanced antioxidant activity of PDA@CeO_2, it still showed a noticeable gap compared to the positive control group (VC). This difference may be attributed to the fact that VC is a well-established and highly efficient antioxidant, and PDA@CeO_2 may not fully match its potency. These findings confirm that PDA@CeO_2 exhibits strong antioxidant capacity, contributing to the reduction of oxidative stress through its ability to absorb and neutralize reactive species.

Cytotoxicity and Safety Assessment of PDA@CeO_2

The CCK-8 assay results showed that after 24 hours of exposure to PDA@CeO_2 NPs (concentrations ranging from 0 to 2000 μg/mL), the survival rates of HSC-T6 remained above 96%, with no significant statistical differences between the concentration groups ($P > 0.05$), as shown in Figure 2A. This indicates that PDA@CeO_2 NPs have minimal cytotoxicity and exhibit good biosafety. In contrast, CeO_2 NPs exhibited higher toxicity, with cell viability significantly reduced at higher concentrations, reaching only 76% at 1000 μg/mL. These results indicate that the inclusion of PDA improves the biocompatibility and safety of the composite material. Furthermore, for HUVEC cells incubated with PDA@CeO_2 NPs, the survival rate remained above 95%, even when the concentration reached 2000 μg/mL, further supporting the biocompatibility of PDA@CeO_2 NPs (Figure SI 1B).

Intracellular ROS Elimination by PDA@CeO_2 NPs

As shown in Figure 2B, we used DCFH-DA as a fluorescent probe to assess ROS levels. A significant increase in ROS was observed following TGF-β1 stimulation. However, CeO_2, PDA, and PDA@CeO_2 NPs all reduced ROS levels, with the most pronounced effect observed in the PDA@CeO_2 NPs. Flow cytometry analysis further confirmed that PDA@CeO_2 significantly reduced ROS levels (Figure 2C). Additionally, the analysis shown in Figure SI 1C indicated that PDA@CeO_2 scavenged ROS significantly more effectively than individual PDA and CeO_2 NPs, highlighting the enhanced antioxidant effect of the composite. The ROS scavenging activity of the PDA@CeO_2 group was significantly greater than that of the TGF-β1-treated group.

PDA@CeO_2 Inhibited the Activation and Migration of HSC-T6 Cells

HSC-T6 cell migration was photographed at 0 and 24 hours following scratching with sterile pipette tips. The relative migration rate was calculated based on the wound area. The results indicated that TGF-β1 enhanced HSC-T6 cell migration, suggesting HSC activation, whereas PDA@CeO_2 significantly inhibited migration at 24 hours (Figure 2D). Supplementary data from the scratch assay (n = 3) can be found in Figure SI 2. The data in Figure 2E show that

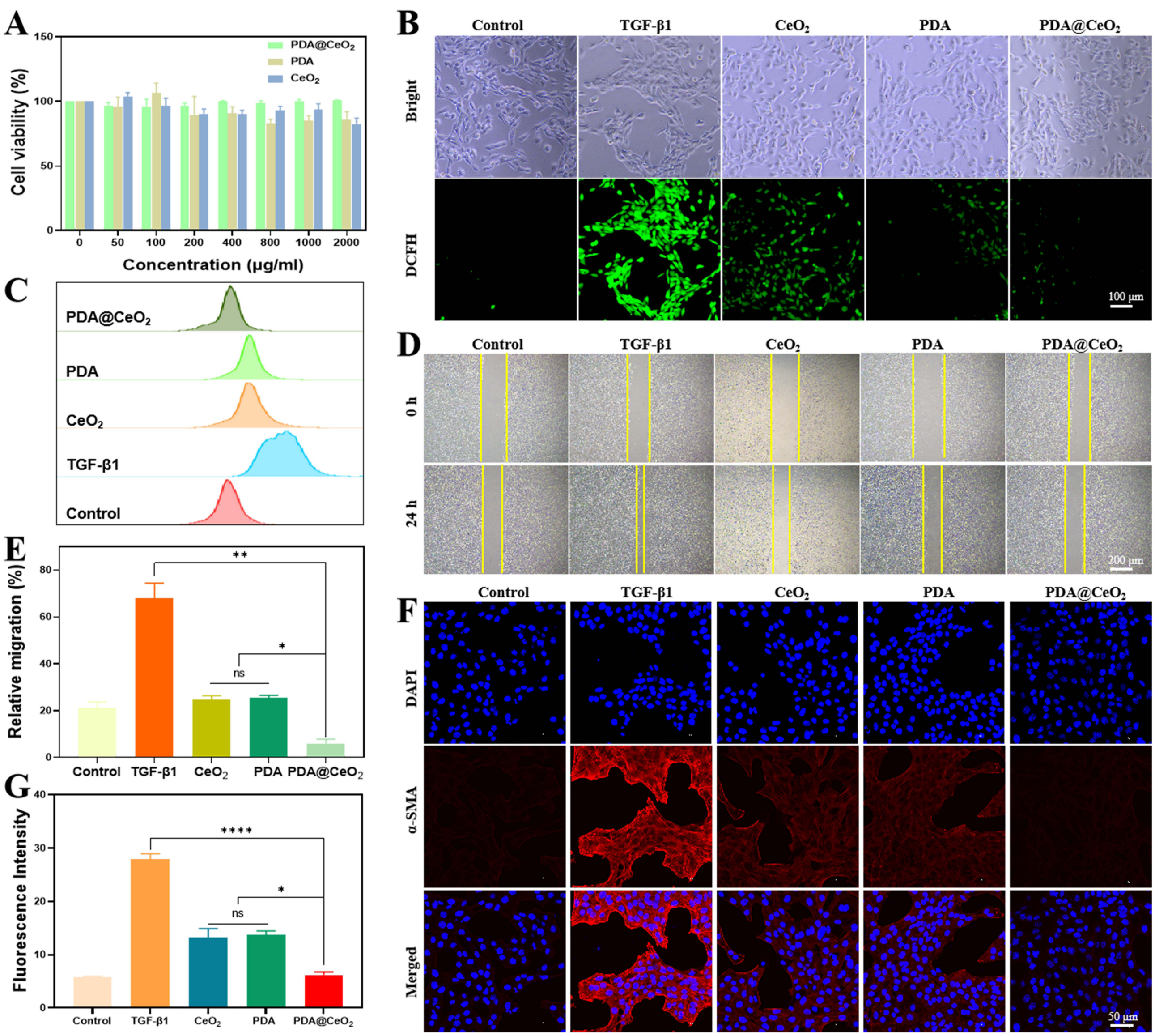

Figure 2 (**A**) Cytotoxicity of CeO$_2$, PDA, and PDA@CeO$_2$ on HSC-T6 cells at different concentrations. The results are presented as the mean ± standard deviation (n = 3). (**B**) ROS scavenging by CeO$_2$, PDA, and PDA@CeO$_2$ in TGF-β1-stimulated HSC-T6 cells. The results are presented as the mean ± standard deviation (n = 3). (**C**) Flow cytometric of ROS clearance by CeO$_2$, PDA, and PDA@CeO$_2$ in TGF-β1-stimulated HSC-T6 cells. The results are presented as the mean ± standard deviation (n = 3). (**D**) Microscopic images of HSC-T6 migration induced by TGF-β1 after treatment with CeO$_2$, PDA, and PDA@CeO$_2$. Data are presented as the mean ± standard deviation (n=3). (**E**) Bar chart showing the statistical analysis of cell migration in different groups. Data are presented as the mean ± standard deviation (n=3). Statistical significance is indicated as ns (no significance), *$P < 0.05$, **$P < 0.01$. (**F**) Confocal microscopy images showing α-SMA expression in TGF-β1-stimulated HSC-T6 cells treated with CeO$_2$, PDA, and PDA@CeO$_2$ (n = 3). (**G**) Fluorescence analysis of α-SMA in hepatic stellate cells treated with CeO$_2$, PDA, and PDA@CeO$_2$ in different groups. Data are presented as the mean ± standard deviation (n=3). Statistical significance is indicated as ns (no significance), *$P < 0.05$, and ****$P < 0.0001$.

PDA@CeO$_2$ significantly inhibited hepatic stellate cell migration, with a statistically significant difference compared to the TGF-β1-only stimulation group. No significant difference was observed between the PDA group and the CeO$_2$ group, but PDA@CeO$_2$ exhibited a significant difference when compared to both the PDA and CeO$_2$ groups. Confocal microscopy results also demonstrated that α-SMA expression in TGF-β1-activated HSC-T6 cells significantly decreased after treatment with PDA@CeO$_2$, indicating that PDA@CeO$_2$ effectively attenuates hepatic stellate cell activation (Figure 2F). The data in Figure 2G are consistent with the aforementioned experimental results. No significant difference was observed between the PDA group and the CeO$_2$ group, while PDA@CeO$_2$ showed significant differences compared to both the PDA and CeO$_2$ groups. PDA@CeO$_2$ significantly reduced α-SMA expression in hepatic stellate cells, with statistical analysis yielding $P < 0.0001$.

Transwell Assay Results

The Transwell migration assay results revealed a significant difference in cell migration between the experimental groups (Figure SI 3). Under normal conditions (control group), only a few cells migrated to the lower surface of the membrane, indicating minimal cell migration. Upon stimulation with TGF-β1, cell migration was notably increased, suggesting that TGF-β1 promotes cell movement. In contrast, the treatment with CeO_2, PDA, and PDA@CeO_2 all resulted in a reduction in the number of migrating cells compared to the TGF-β1 stimulated group. Among these treatments, PDA@CeO_2 exhibited the strongest inhibitory effect on cell migration, followed by PDA and CeO_2. Statistical analysis showed a significant difference in cell migration between the control group, TGF-β1 treated group, and the experimental treatment groups (CeO_2, PDA, PDA@CeO_2). The PDA@CeO_2 group had the most pronounced reduction in migration, with statistical significance compared to both the TGF-β1 and other treatment groups. The CeO_2 and PDA groups also showed significant inhibition of migration, though to a lesser extent than PDA@CeO_2. These results suggest that while TGF-β1 stimulates cell migration, CeO_2, PDA, and PDA@CeO_2 effectively suppress migration, with PDA@CeO_2 being the most potent inhibitor.

Cellular Uptake of DiI-Labeled PDA@CeO_2 NPs

After co-culturing DiI-labeled PDA@CeO_2 with hepatocytes, activated HSC-T6 cells (treated with 5 ng/mL TGF-β1 for 12 hours), and HSC-T6 cells for 6 hours, the confocal microscopy results in Figure 3A demonstrate that all three cell types are capable of internalizing PDA@CeO_2. Further flow cytometry analysis (Figure 3B) similarly shows that activated HSC-T6 cells exhibit the highest uptake rate. However, no statistically significant difference was observed between activated and non-activated HSC-T6 cells, while hepatocytes exhibited the lowest uptake rate compared to the other two groups, with a significant difference ($P < 0.001$). The statistical data histogram can be found in Supplementary Information (SI 4). Differences in metabolic pathways and energy consumption between hepatocytes and HSC-T6 cells may contribute to the observed differences in uptake. HSC-T6 cells likely internalize PDA@CeO_2 more efficiently through enhanced endocytosis, whereas hepatocytes may have a lower endocytic activity or slower metabolic rate, limiting their uptake capacity. Moreover, the lack of a statistically significant difference in uptake between activated and non-activated HSC-T6 cells could be attributed to the heterogeneity within the HSC-T6 cell population. Even after activation, the cells may be in different activation states, and this heterogeneity could account for the absence of significant differences in uptake between these groups.

Safety Assessment of PDA@CeO_2 in vivo

The biocompatibility of PDA, CeO_2, and PDA@CeO_2 was evaluated by monitoring the body weight changes of experimental animals over a specified period. No significant difference in body weight was observed between the PDA, CeO_2, and PDA@CeO_2-treated groups and the control group, suggesting that these materials had no notable adverse effects on overall health during the observation period (Figure 4A). The hemolytic activity of PDA, CeO_2, and PDA@CeO_2 was assessed by measuring the hemolysis rate. The results showed that the hemolysis rates for all tested materials were below 5%, indicating minimal or negligible hemolytic activity. These results suggest that the materials are non-hemolytic and have good blood compatibility (Figures 4B and SI 5A). To evaluate the systemic toxicity of CeO_2, PDA, and PDA@CeO_2 in rats, normal rats were intravenously injected with CeO_2, PDA, and PDA@CeO_2 for four weeks. Subsequently, H&E staining was performed on the heart, liver, spleen, lungs, and kidneys. The results indicated no notable abnormalities in the H&E staining of the CeO_2, PDA, and PDA@CeO_2 groups in the normal rats (Figure 4C). Serological tests revealed that serum ALT and AST levels were significantly elevated in the model group compared to the control group, whereas these levels were significantly reduced in the PDA@CeO_2 group, indicating a protective effect on liver function. Additionally, the levels of alanine aminotransferase and aspartate aminotransferase in the PDA@CeO_2 group were significantly lower than those in the model group. No significant differences in renal function test results were observed between the groups (Figure 4D).

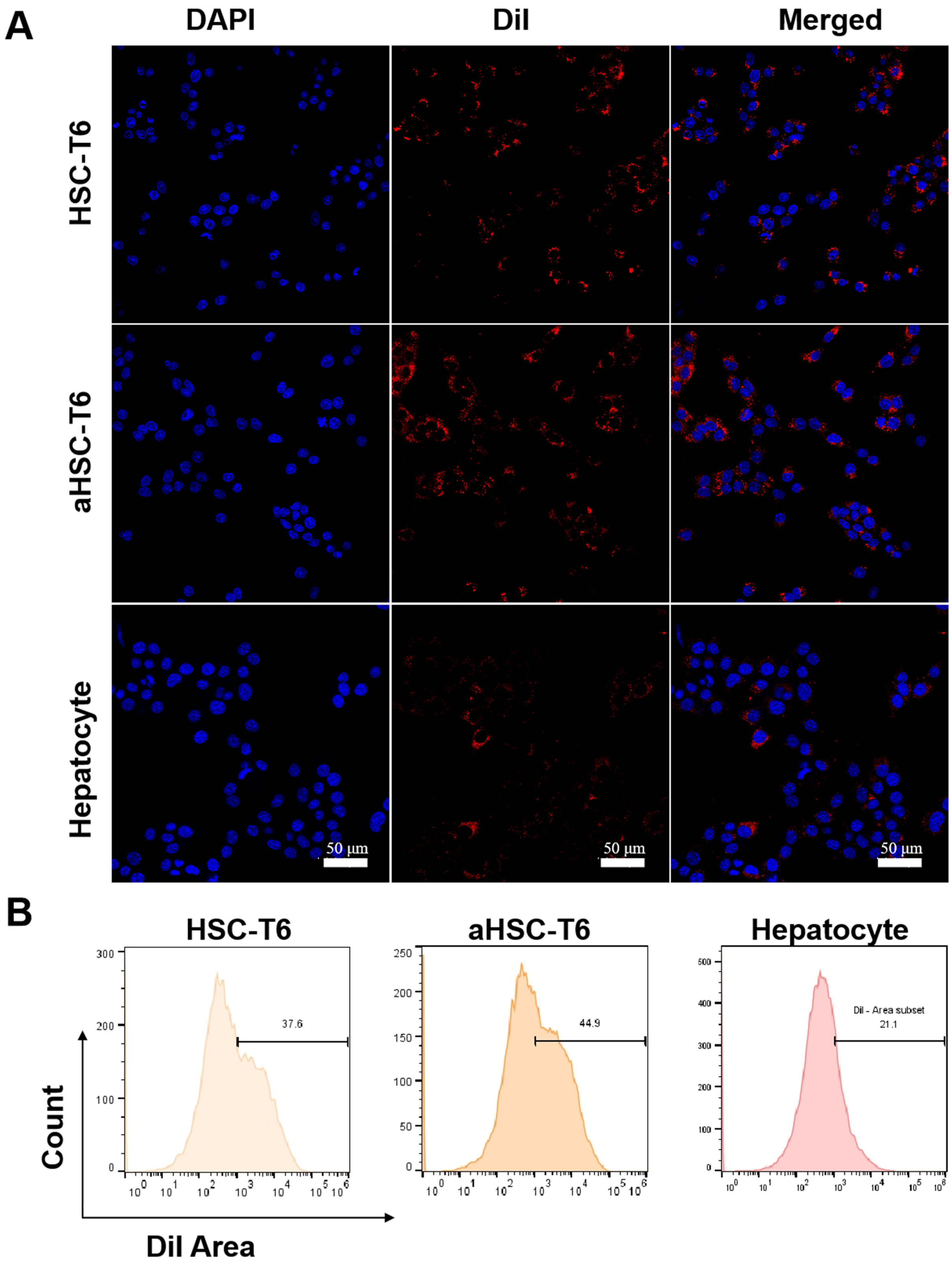

Figure 3 (**A**) Confocal microscopy images showing the uptake of DiI-labeled PDA@CeO$_2$ by HSC-T6, TGF-β1-stimulated HSC-T6, and hepatocytes. The scale bar represents 50 μm. Data are presented as the mean ± standard deviation (n=3). (**B**) Flow cytometry analysis of DiI-labeled PDA@CeO$_2$ uptake by HSC-T6, TGF-β1-stimulated HSC-T6, and hepatocytes. Data are presented as the mean ± standard deviation (n=3).

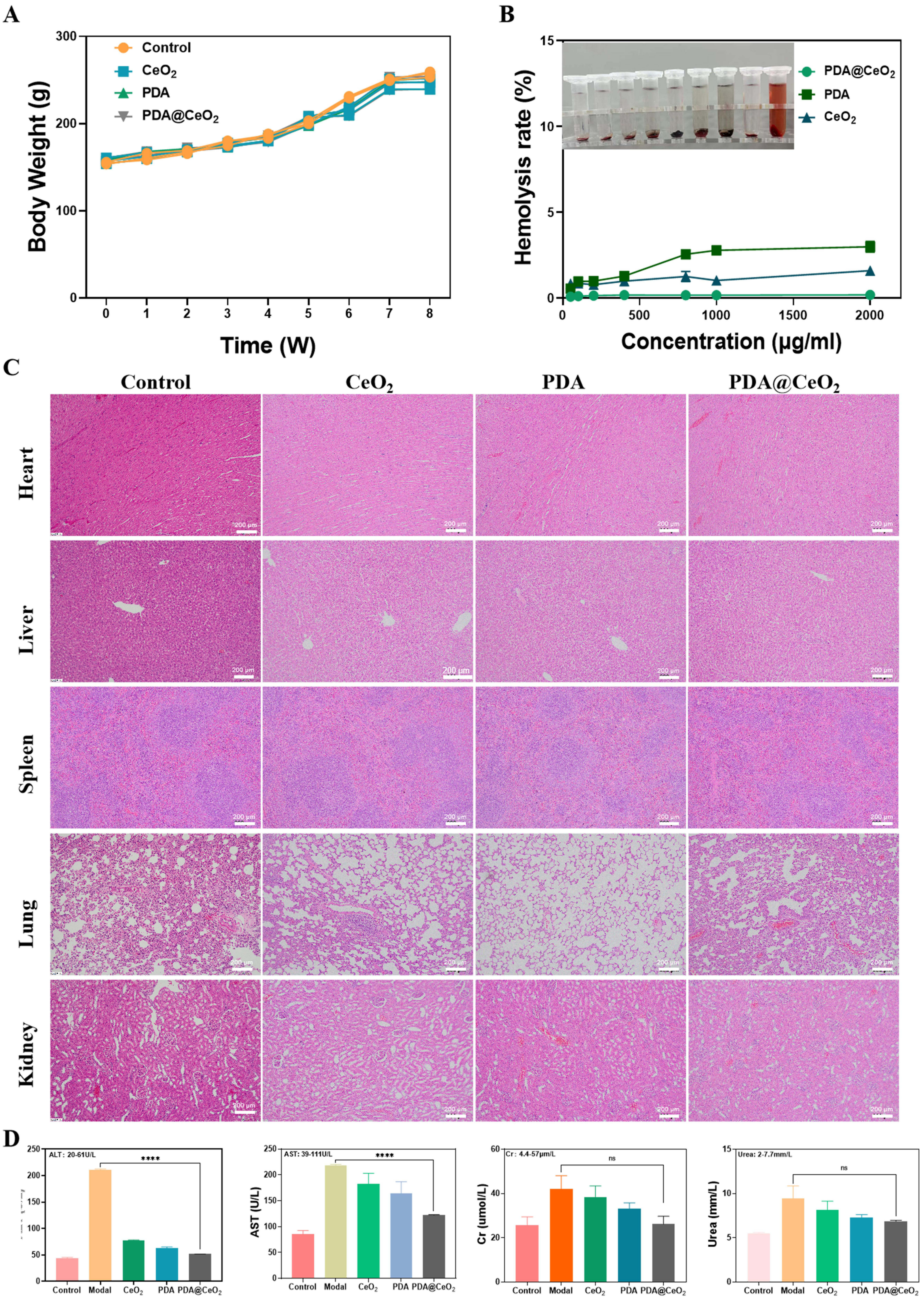

Figure 4 (**A**) Line graph showing the body weight changes in different groups treated with PDA, CeO_2, and $PDA@CeO_2$. Data are presented as the mean ± standard deviation (n=5). (**B**) Line graph showing the hemolysis assay results for different groups treated with PDA, CeO_2, and $PDA@CeO_2$. Data are presented as the mean ± standard deviation (n=3). (**C**) H&E staining of heart, liver, spleen, lung, and kidney tissues from normal rats and rats treated with PDA, CeO_2, and $PDA@CeO_2$, captured by microscopy. The scale bar represents 200 μm. Data are presented as the mean ± standard deviation (n=3). This image demonstrates the biological safety of the materials. (**D**) Bar chart showing the analysis of ALT, AST, Cr, and Urea levels in rats from different groups (Control, Modal, CeO_2, PDA, $PDA@CeO_2$). Data are presented as the mean ± standard deviation (n=3). Statistical significance is indicated, with "ns" for no significant difference and ****$P < 0.0001$.

In vivo Distribution of PDA@CeO$_2$ NPs

IR-820-labeled PDA@CeO$_2$ NPs were intravenously injected into rats with liver fibrosis, and imaging was conducted at various time points (4 hours, 8 hours, 12 hours, 24 hours, 48 hours, and 72 hours). The results showed that the fluorescence intensity was highest at 4 hours, and then gradually decreased over time due to metabolic processes in the body, as shown in Figure 5A. Most of the fluorescence accumulated in the liver, indicating that the liver is the primary organ for nanoparticle accumulation. Imaging of the heart, liver, spleen, lungs, and kidneys at different time points yielded consistent results, further confirming the predominant role of the liver in nanoparticle distribution. As shown in Figure 5B, these imaging results further illustrate the liver's dominant role in the accumulation of nanoparticles. Over time, the nanoparticles were metabolized and cleared from the bloodstream, leading to a gradual reduction in fluorescence intensity. These findings suggest that the liver exhibits a significant affinity for the uptake of PDA@CeO$_2$ NPs, and the in vivo metabolic processes play a crucial role in determining their biological distribution.

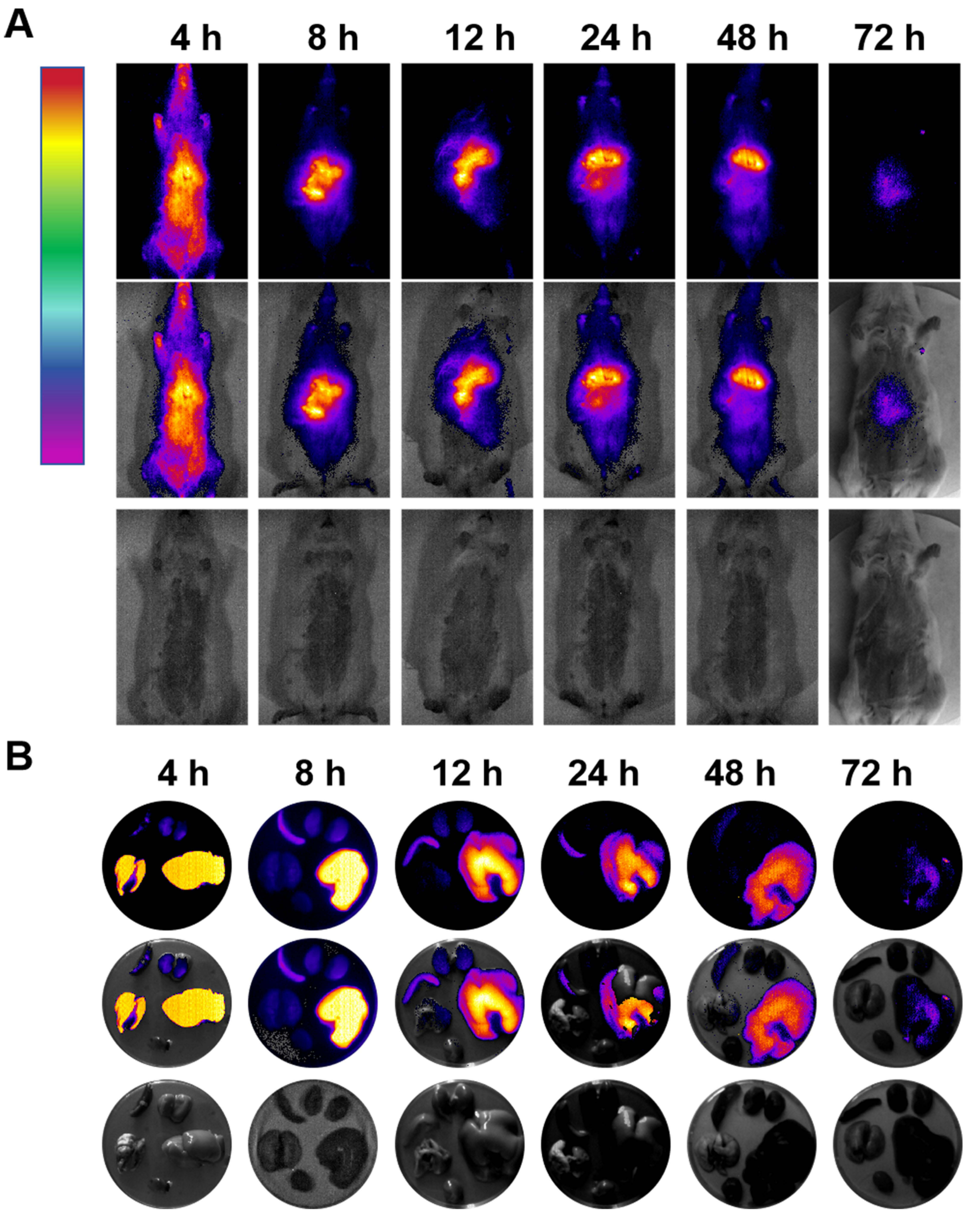

Figure 5 (**A**) In vivo small animal imaging of rats injected with IR820-labeled PDA@CeO$_2$ at different time points (4h, 8h, 12h, 24h, 48h, 72h). Data are presented as the mean ± standard deviation (n=3). (**B**) Imaging of heart, liver, spleen, lung, and kidney tissues from rats injected with IR820-labeled PDA@CeO$_2$ at different time points (4h, 8h, 12h, 24h, 48h, 72h). Data are presented as mean ± standard deviation (n=3).

2D Shear Wave Elastography in Rat Liver Fibrosis Models

To confirm the successful establishment of the rat liver fibrosis model, 2D-SWE was performed before (0 weeks) and at 4, 6, and 8 weeks after carbon tetrachloride injection. Histological analysis showed progressive fibrosis: at week 4, H&E staining revealed mild hepatocyte swelling and fatty degeneration; at week 6, inflammatory cell infiltration and hepatocyte necrosis; by week 8, significant fibrosis and liver structural damage (Figure 6A). Masson's trichrome staining showed a gradual increase in collagen deposition, indicating mild fibrosis at week 4, moderate fibrosis at week 6, and severe fibrosis or cirrhosis at week 8 (Figure 6B). Sirius Red staining mirrored this progression, with mild fibrosis at week 4, moderate fibrosis at week 6, and advanced fibrosis or cirrhosis by week 8 (Figure 6C). The 2D-SWE results demonstrated a corresponding increase in liver stiffness: from 7.46 ± 0.76 kPa at week 0 (normal) to 11.49 ± 1.33 kPa at week 4 (mild fibrosis), 18.81 ± 2.38 kPa at week 6 (moderate fibrosis), and 18.93 ± 1.74 kPa at week 8 (severe fibrosis or cirrhosis) (Figure 6D). Statistically significant differences in 2D-SWE were observed at week 4 ($P < 0.05$) compared to the control group (Figure 6E). These findings suggest a clear correlation between increased liver stiffness and fibrosis progression.

Anti-Liver Fibrosis Effect of PDA@CeO$_2$ in vivo

Based on these findings, we selected 4 weeks as the optimal time point to initiate liver fibrosis treatment. At this stage, mild fibrosis has already developed, and the use of PDA@CeO$_2$ for antioxidant stress treatment can help prevent further progression of the disease before it advances to moderate or severe stages. This approach may help prevent the liver from progressing to more severe fibrosis or cirrhosis. Subsequently, experiments were conducted 4 weeks after subcutaneous injection of carbon tetrachloride. The animals were divided into different groups: the control group, the liver fibrosis model group (receiving bi-weekly subcutaneous injections of carbon tetrachloride for 8 weeks, followed by tail vein injection of PBS starting from week 4), and the treatment groups (receiving bi-weekly subcutaneous injections of carbon tetrachloride for 8 weeks, with intravenous injections of CeO$_2$, PDA, or PDA@CeO$_2$ twice a week starting from week 4). The treatment schedule is shown in Figure 7A.

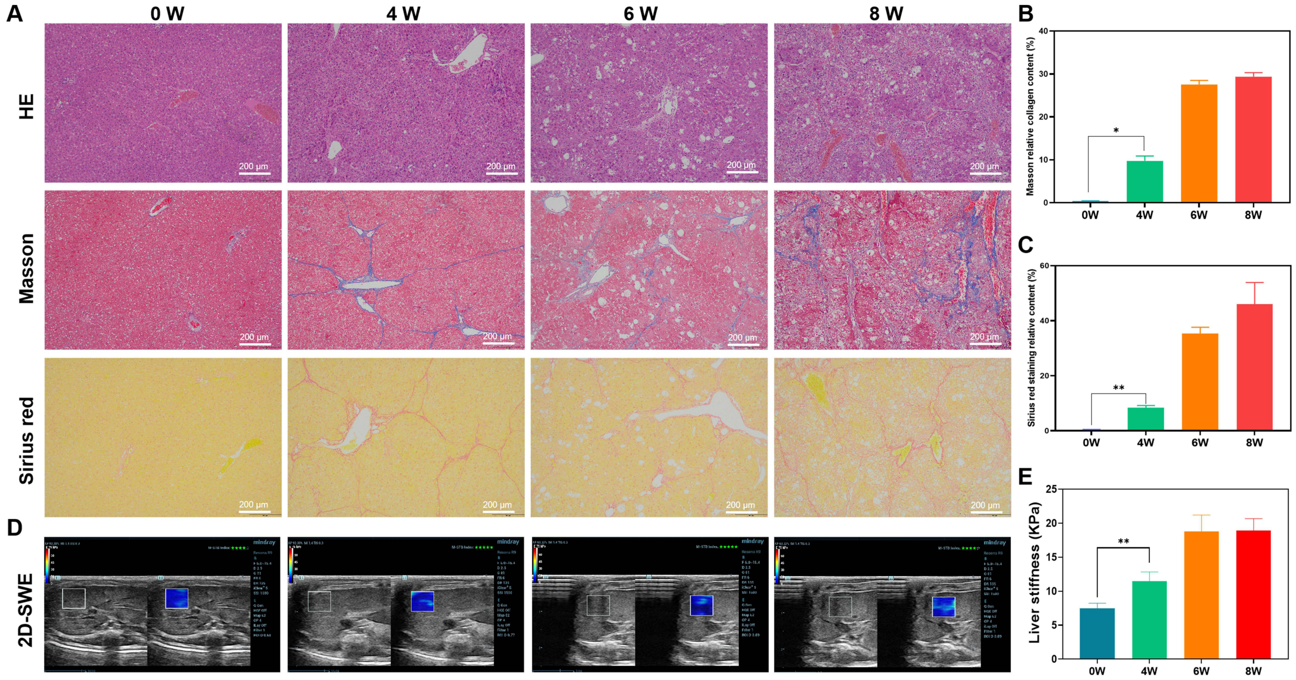

Figure 6 (**A**) Histological analysis of liver fibrosis in rats at 0W, 4W, 6W, and 8W post-CCL4 injection (H&E, Sirius Red, and Masson staining, n=3), with a scale bar of 200 μm. Data are presented as mean ± standard deviation. (**B**) Analysis of Masson staining results (n=3). Data are presented as mean ± standard deviation. (**C**) Analysis of Sirius Red staining results (n=3). Data are presented as mean ± standard deviation. (**D**) Ultrasound image of two-dimensional shear wave elastography (n=5). Data are presented as mean ± standard deviation. (**E**) Analysis of two-dimensional shear wave elastography data at different weeks (n=5). Data are presented as mean ± standard deviation. Statistical significance is indicated as *$P < 0.05$ and **$P < 0.01$.

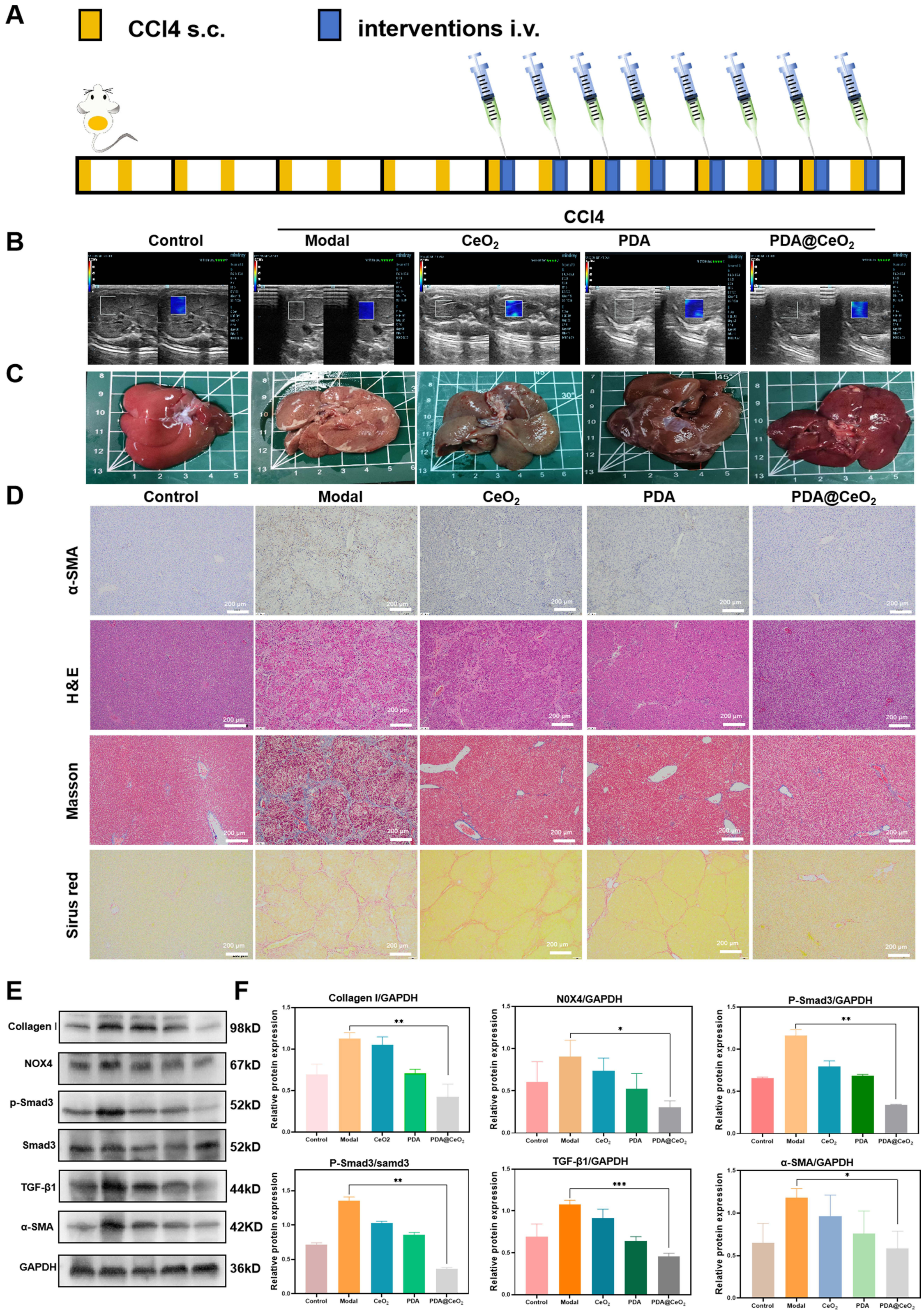

Figure 7 (**A**) Schematic representation of the treatment process. (**B**) Ultrasound elastography images post-treatment (n=5). Data are expressed as the mean ± standard deviation. (**C**) Liver morphological changes after treatment (n=5). Data are expressed as the mean ± standard deviation. (**D**) Histological analysis of liver tissue (H&E, Sirius Red, Masson, α-SMA staining) (n=3). Data are expressed as the mean ± standard deviation, with a scale bar of 200 μm. (**E**) Western blot analysis of protein expression (n=3). Data are expressed as the mean ± standard deviation. (**F**) Protein expression analysis of Collagen I, α-SMA, TGF-β1, p-SMAD3, and NOX4 (n=3). Data are expressed as the mean ± standard deviation. Statistical significance was determined as *$P < 0.05$, **$P < 0.01$, and ***$P < 0.001$.

https://doi.org/10.2147/IJN.S521372

To evaluate the effect of PDA, CeO_2, and PDA@CeO_2 on the progression of liver fibrosis, the liver elasticity values of rats in different treatment groups were measured at 0, 4, 6, and 8 weeks, as shown in Figures 7B and SI 5B. At the end of the treatment, the baseline elasticity value of the control group was 6.87 ± 1.29 kPa, indicating normal liver stiffness. In contrast, the liver stiffness in the model group significantly increased, with an elasticity value of 21.62 ± 1.97 kPa. In the treatment groups, the CeO_2 group showed a moderate decrease in liver stiffness, with an elasticity value of 18.25 ± 2.76 kPa, indicating some alleviation of fibrosis. Similarly, the PDA group showed a reduction in liver stiffness to 16.64 ± 0.67 kPa, suggesting a certain therapeutic effect. The PDA@CeO_2 group demonstrated the most significant improvement, with the elasticity value further reduced to 13.64 ± 1.97 kPa, suggesting that the synergistic effect between PDA and CeO_2 played a key role in alleviating liver fibrosis (Figure SI 5C). Liver morphology was then examined macroscopically, and compared to the control group, the carbon tetrachloride model group displayed typical features of liver fibrosis. Moreover, the liver appearance and fibrotic morphology in the PDA@CeO_2 group appeared smoother compared to the model group (Figure 7C). Subsequently, liver tissues from different groups were subjected to α-SMA immunohistochemical staining, as well as H&E, Masson, and Sirius Red staining for further analysis.

As shown in Figure 7D, α-SMA immunohistochemical staining revealed a significant reduction in α-SMA expression in the PDA@CeO_2-treated group, indicating substantial inhibition of myofibroblast activation and fibrosis formation. H&E staining further demonstrated severe liver damage in the model group, including destruction of lobular architecture, disarray of hepatic cords, inflammatory cell infiltration, and hepatocyte edema. In contrast, the PDA@CeO_2-treated group showed marked structural recovery, with more ordered hepatic cord arrangement resembling normal tissue. These findings were corroborated by Masson's trichrome staining, which showed pronounced collagen deposition and extensive fibrous proliferation in the portal areas of the model group, accompanied by widespread fibrous septa and pseudolobule formation. In comparison, the PDA@CeO_2-treated group exhibited significant reduction in fibrosis, with thinner fibrous septa and less collagen deposition. Similarly, Sirius Red staining demonstrated a notable decrease in collagen deposition in the PDA@CeO_2-treated group, further confirming its significant therapeutic effect in alleviating liver fibrosis. Figure SI 6A shows α-SMA immunohistochemical analysis, indicating a significant reduction in α-SMA expression in the PDA@CeO_2 group, reflecting a marked decrease in myofibroblast activity with statistical significance. Figure SI 6B presents Masson's trichrome staining, where the PDA@CeO_2 group showed substantially reduced collagen deposition compared to the model group. Finally, Figure SI 6C displays Sirius Red staining, confirming that PDA@CeO_2 treatment significantly reduced collagen fiber accumulation in the treated rats compared to the model group, effectively mitigating liver fibrosis with statistical significance.

Regulation of the TGF-β/RSMADS/ISMADS Balance to Suppress HSC Activation in vivo

Clearing excessive ROS and modulating the TGF-β/Smad3 pathway are key strategies for treating liver fibrosis. Western blot analysis demonstrated that PDA@CeO_2 treatment significantly reduced the expression of NOX4, a marker associated with oxidative stress, in liver fibrosis tissues. Additionally, PDA@CeO_2 treatment notably decreased TGF-β1 levels during the progression of liver fibrosis, likely due to the removal of ROS, which reduced the activation of HSC-T6 cells and consequently lowered TGF-β1 secretion. Compared to PDA and CeO_2 treatments alone, PDA@CeO_2 significantly decreased the expression levels of Collagen I, α-SMA, TGF-β1, p-SMAD3, and NOX4 (Figure 7E). Notably, the levels of Collagen I and α-SMA in the PDA@CeO_2 group were markedly lower, indicating reduced fibrosis and decreased activation of myofibroblasts. The expression of TGF-β1 and p-SMAD3 was also significantly reduced, suggesting inhibition of the TGF-β1/SMAD3 pathway. Furthermore, NOX4 expression was significantly downregulated, highlighting the antioxidant effect of the treatment. Quantitative analysis confirmed that the levels of Collagen I and α-SMA in the PDA@CeO_2 group were significantly lower than those in the PDA and CeO_2 groups, with statistical significance, indicating that PDA@CeO_2 effectively alleviated fibrosis and inhibited myofibroblast activation. In conclusion, these findings underscore the therapeutic efficacy of PDA@CeO_2 in modulating key fibrosis markers and oxidative stress pathways, with all differences showing statistical significance (Figure 7F).

Discussion and Conclusion

This study explored the intracellular antioxidant mechanisms of PDA@CeO_2 NPs, which possess ROS scavenging capabilities. The PDA@CeO_2 NPs, synthesized using a simple method, demonstrated a uniform size distribution and excellent biocompatibility, making them suitable for potential biomedical applications. Fluorescence imaging confirmed that these nanoparticles effectively scavenged intracellular ROS, providing evidence of their antioxidative capacity.

Furthermore, our results demonstrate that PDA@CeO_2 NPs alleviate TGF-β1-induced activation of HSC-T6 cells and partially restore oxidative balance through the NOX4/ROS pathway. This mechanism inhibits the proliferation and migration of hepatic stellate cells, which are key processes in preventing the further progression of liver fibrosis. However, other potential mechanisms underlying the therapeutic effects of PDA@CeO_2 NPs still require further investigation. These findings suggest that PDA@CeO_2 NPs hold significant potential in the treatment of liver fibrosis, although additional research is necessary to fully elucidate their mode of action.[41,42] In this study, we utilized the HSC-T6 cell line derived from rats, as validating the effects of nanomaterials in human models is challenging. The carbon tetrachloride (CCl_4)-induced rat liver fibrosis model is widely adopted in such studies, providing reliable in vivo validation.[43,44] To assess the therapeutic effects of PDA@CeO_2 in liver fibrosis in vivo, we employed subcutaneous injection of CCl_4 to induce fibrosis. However, this method differs from the primary causes of human liver fibrosis, such as non-alcoholic or metabolic-associated fatty liver diseases (NAFLD/NASH), which are driven by long-term fat accumulation, insulin resistance, and chronic low-grade inflammation. This discrepancy highlights an important avenue for future research. Moreover, since rat hepatic stellate cells may not fully represent the physiological characteristics of humans, we plan to use human-derived hepatic stellate cell lines in future studies. This will help us better understand the therapeutic effects and mechanisms of PDA@CeO_2 NPs in human liver fibrosis.

Moreover, we incorporated 2D-SWE in our study to assess liver fibrosis progression and monitor the therapeutic effects of PDA@CeO_2 NPs. 2D-SWE, a non-invasive imaging technique that measures tissue stiffness, played a critical role in assessing the extent of liver fibrosis and evaluating the efficacy of the treatment. While 2D-SWE provides real-time, quantitative data on liver stiffness, it does have some limitations, such as susceptibility to operator variability and difficulties in assessing areas with heterogeneous liver tissue or significant steatosis. However, we took care to minimize these potential sources of error during the experiment by standardizing the imaging protocols and ensuring consistent operator training. These measures helped reduce variability and enhance the reliability and accuracy of the results, further supporting the potential of PDA@CeO_2 in reducing liver stiffness.

In our liver fibrosis animal model, we chose 4W as the treatment time point because significant histopathological changes and statistical differences in fibrosis markers typically emerge by this time. At 4W, fibrosis progression was advanced enough to assess the therapeutic effects of PDA@CeO_2 NPs, offering a relevant window for evaluation. However, a limitation is that this timeframe may not fully reflect long-term treatment outcomes or the reversal of advanced fibrosis. Despite this, the consistent results at 4W, along with controlled conditions, enhance the reliability of our findings and support the potential of PDA@CeO_2 NPs as an anti-fibrosis therapy.

In conclusion, the combination of PDA@CeO_2 NPs and 2D-SWE offers a promising approach for the treatment and monitoring of liver fibrosis. This study provides the first systematic exploration of the potential of PDA@CeO_2 NPs in anti-fibrotic therapy, particularly highlighting their critical role in intracellular antioxidant mechanisms and the restoration of oxidative balance. We have not only elucidated the mechanisms by which these nanoparticles eliminate ROS, inhibit hepatic stellate cell migration, and alleviate liver fibrosis, but also provided novel theoretical and experimental support for anti-fibrotic treatments. Furthermore, the use of 2D-SWE technology has played a crucial role in the real-time monitoring of liver fibrosis progression and therapeutic effects, significantly enhancing the precision and feasibility of the study. This research not only expands the potential applications of nanomaterials in the biomedical field but also opens up new avenues for future strategies in liver fibrosis treatment.

Data Sharing Statement

The authors are willing to provide the raw data supporting the conclusions of this article upon request, without any unnecessary restrictions. The data supporting the findings of this study are available from the corresponding author upon reasonable request.

Animal Research Statement

All animal experiments conducted in this study were reviewed and approved by the Animal Research Committee of North Sichuan Medical College (Approved Protocol No. [2024028]) and were performed in accordance with the guidelines outlined in the Guide for the Care and Use of Laboratory Animals.

Acknowledgments

This research was funded by the 2024 Annual Research Development Plan Project of the Affiliated Hospital of Clinical Medical College, North Sichuan Medical College (Grant No: 2024PTZK013). This study is funded by the Sichuan Provincial Natural Science Youth Fund Project (Grant No: 2024NSFSC1896).

Disclosure

The authors confirm that there are no commercial or financial interests that could be considered a conflict in relation to this study.

References

1. Lackner C, Tiniakos D. Fibrosis and alcohol-related liver disease. *J Hepatol*. 2019;70(2):294–304. doi:10.1016/j.jhep.2018.12.003
2. Hammerich L, Tacke F. Hepatic inflammatory responses in liver fibrosis. *Nat Rev Gastroenterol Hepatol*. 2023;20(10):633–646. doi:10.1038/s41575-023-00807-x
3. Chen L, Guo W, Mao C, Shen J, Wan M. Liver fibrosis: pathological features, clinical treatment and application of therapeutic nanoagents. *J Mat Chem B*. 2024;12(6):1446–1466. doi:10.1039/D3TB02790B
4. Shinn J, Park S, Lee S, et al. Antioxidative hyaluronic acid-bilirubin nanomedicine targeting activated hepatic stellate cells for anti-hepatic-fibrosis therapy. *ACS nano*. 2024;18(6):4704–4716. doi:10.1021/acsnano.3c06107
5. Bai Y, Chen J, Zhang S, et al. Inflammation-responsive cell membrane-camouflaged nanoparticles against liver fibrosis via regulating endoplasmic reticulum stress and oxidative stress. *Adv Mater*. 2024;36(19):e2310443. doi:10.1002/adma.202310443
6. Li HM, Feng LL, Jiang Q, et al. A novel nanoscale phase-change contrast agent evaluates the hepatic fibrosis through targeting hepatic stellate cell platelet-derived factor beta receptor by ultrasound in vitro. *Ultrasound Med Biol*. 2024;51(3):508–518.
7. Lin YL, Wu CF, Huang YT. Effects of rhubarb on migration of rat hepatic stellate cells. *J Gastroenterol Hepatol*. 2009;24(3):453–461. doi:10.1111/j.1440-1746.2008.05573.x
8. Gandhi CR. Hepatic stellate cell activation and pro-fibrogenic signals. *J Hepatol*. 2017;67(5):1104–1105. doi:10.1016/j.jhep.2017.06.001
9. Higashi T, Friedman SL, Hoshida Y. Hepatic stellate cells as key target in liver fibrosis. *Adv Drug Delivery Rev*. 2017;121:27–42. doi:10.1016/j.addr.2017.05.007
10. Jin FC, Chen JJ, Xu QX, et al. Kinetin inhibits hepatic stellate cell activation and induces apoptosis via interactions with the TGF-β1/Smad signaling pathway. *Toxicol Appl Pharmacol*. 2023;475:116655. doi:10.1016/j.taap.2023.116655
11. Bernard K, Thannickal VJ. NADPH Oxidase Inhibition in Fibrotic Pathologies. *Antioxid Redox Signaling*. 2020;33(6):455–479. doi:10.1089/ars.2020.8032
12. Herranz-Itúrbide M, Peñuelas-Haro I, Espinosa-Sotelo R, Bertran E, Fabregat I. The TGF-β/NADPH oxidases axis in the regulation of liver cell biology in health and disease. *Cells*. 2021;10(9):2312. doi:10.3390/cells10092312
13. Liang S, Kisseleva T, Brenner DA. The role of NADPH Oxidases (NOXs) in liver fibrosis and the activation of myofibroblasts. *Front Physiol*. 2016;7:17. doi:10.3389/fphys.2016.00017
14. Baghaei K, Mazhari S, Tokhanbigli S, et al. Therapeutic potential of targeting regulatory mechanisms of hepatic stellate cell activation in liver fibrosis. *Drug Discov Today*. 2022;27(4):1044–1061. doi:10.1016/j.drudis.2021.12.012
15. Blas-García A, Apostolova N. Novel therapeutic approaches to liver fibrosis based on targeting oxidative stress. *Antioxidants*. 2023;12(8):1567. doi:10.3390/antiox12081567
16. Tang Z, Li X, Tian L, Sun Y, Zhu X, Liu F. Mesoporous polydopamine based biominetic nanodrug ameliorates liver fibrosis via antioxidation and TGF-β/SMADS pathway. *Int J Biol Macromol*. 2023;248:125906. doi:10.1016/j.ijbiomac.2023.125906
17. Xu Y, Zhou X, Wang X, Jin Y, Zhou L, Ye J. Progress of mesenchymal stem cells (MSCs) & MSC-Exosomes combined with drugs intervention in liver fibrosis. *Biomed Pharmacother*. 2024;176:116848. doi:10.1016/j.biopha.2024.116848
18. Luan J, Li R, Xu W, et al. Functional biomaterials for comprehensive periodontitis therapy. *Acta Pharm Sin B*. 2023;13(6):2310–2333. doi:10.1016/j.apsb.2022.10.026
19. Lin L, Gong H, Li R, et al. Nanodrug with ROS and pH dual-sensitivity ameliorates liver fibrosis via multicellular regulation. *Adv Sci*. 2020;7(7):1903138. doi:10.1002/advs.201903138
20. Qin S, Du X, Wang K, et al. Vitamin A-modified ZIF-8 lipid nanoparticles for the therapy of liver fibrosis. *Int J Pharm*. 2023;642:123167. doi:10.1016/j.ijpharm.2023.123167
21. Sun Y, Xu T, Qian Y, et al. NOS-like activity of CeO(2) nanozymes contributes to diminishing the vascular plaques. *J Nanobiotechnol*. 2024;22(1):12. doi:10.1186/s12951-023-02276-5
22. Chen MW, Lu QJ, Chen YJ, et al. NIR-PTT/ROS-scavenging/oxygen-enriched synergetic therapy for rheumatoid arthritis by a pH-responsive hybrid CeO(2)-ZIF-8 coated with polydopamine. *ACS Biomater Sci Eng*. 2022;8(8):3361–3376. doi:10.1021/acsbiomaterials.2c00592
23. Wu Y, Ta HT. Different approaches to synthesising cerium oxide nanoparticles and their corresponding physical characteristics, and ROS scavenging and anti-inflammatory capabilities. *J Mat Chem B*. 2021;9(36):7291–7301. doi:10.1039/D1TB01091C

24. Li X, Qi M, Li C, et al. Novel nanoparticles of cerium-doped zeolitic imidazolate frameworks with dual benefits of antibacterial and anti-inflammatory functions against periodontitis. *J Mat Chem B*. 2019;7(44):6955–6971. doi:10.1039/C9TB01743G
25. Kobyliak N, Virchenko O, Falalyeyeva T, et al. Cerium dioxide nanoparticles possess anti-inflammatory properties in the conditions of the obesity-associated NAFLD in rats. *Biomed Pharmacother*. 2017;90:608–614. doi:10.1016/j.biopha.2017.03.099
26. Fernández-Varo G, Perramón M, Carvajal S, et al. Bespoken nanoceria: an effective treatment in experimental hepatocellular carcinoma. *Hepatology*. 2020;72(4):1267–1282. doi:10.1002/hep.31139
27. Lai C, Yan H, Wang D, et al. Facile synthesis of Mn, Ce co-doped g-C(3)N(4) composite for peroxymonosulfate activation towards organic contaminant degradation. *Chemosphere*. 2022;293:133472. doi:10.1016/j.chemosphere.2021.133472
28. Eilenberger C, Selinger F, Rothbauer M, et al. Cytotoxicity, retention, and anti-inflammatory effects of a CeO(2) nanoparticle-based supramolecular complex in a 3D liver cell culture model. *ACS Pharmacol Transl Sci*. 2021;4(1):101–106. doi:10.1021/acsptsci.0c00170
29. Gobut H, Kucuk A, Şengel N, et al. Effects of cerium oxide (CeO(2)) on liver tissue in liver ischemia-reperfusion injury in rats undergoing desflurane anesthesia. *BMC Anesthesiol*. 2023;23(1):40. doi:10.1186/s12871-023-01999-0
30. Boey A, Leong SQ, Bhave S, Ho HK. Cerium oxide nanoparticles alleviate hepatic fibrosis phenotypes in vitro. *Int J Mol Sci*. 2021;22(21):11777. doi:10.3390/ijms222111777
31. Shen J, Shi W, Liu G, et al. Early diagnosis and treatment of osteoarthritis with a Au@PDA-WL NP nano-probe by photoacoustic imaging. *J Mat Chem B*. 2023;11(25):5777–5785. doi:10.1039/D3TB00760J
32. Wang Y, Wang X, Liu X, et al. Fabrication, characterization and potential application of biodegradable polydopamine-modified scaffolds based on natural macromolecules. *Int J Biol Macromol*. 2023;253(Pt 1):126596. doi:10.1016/j.ijbiomac.2023.126596
33. Zhang B, Li Q, Xu Q, Li B, Dong H, Mou Y. Polydopamine modified ceria nanorods alleviate inflammation in colitis by scavenging ROS and regulating macrophage M2 polarization. *Int J Nanomed*. 2023;18:4601–4616. doi:10.2147/IJN.S416049
34. Ma Z, Tian X, Yu S, et al. Liver fibrosis amelioration by macrophage-biomimetic polydopamine nanoparticles via synergistically alleviating inflammation and scavenging ROS. *Mol Pharmaceut*. 2024;21(6):3040–3052. doi:10.1021/acs.molpharmaceut.4c00249
35. Guo X, Li Z, Liu S, et al. Studying the effect of PDA@CeO(2) nanoparticles with antioxidant activity on the mechanical properties of cells. *J Mat Chem B*. 2021;9(44):9204–9212. doi:10.1039/D1TB01918J
36. Yin M, Lei D, Liu Y, et al. NIR triggered polydopamine coated cerium dioxide nanozyme for ameliorating acute lung injury via enhanced ROS scavenging. *J Nanobiotechnol*. 2024;22(1):321. doi:10.1186/s12951-024-02570-w
37. Shi X, Li J, Min B, Yang R, He C, Yang Y. Application of ultrasound elastography for monitoring the effects of TβR1 shRNA therapy on hepatic fibrosis in a rat model. *PLoS One*. 2021;16(6):e0253150. doi:10.1371/journal.pone.0253150
38. Kovatsch A, Honcharova-Biletska H, Segna D, et al. Performance of two-dimensional shear wave elastography and transient elastography compared to liver biopsy for staging of liver fibrosis. *Eur J Clin Invest*. 2023;53(7):e13980. doi:10.1111/eci.13980
39. Chen Y, Li J, Zhou Q, Lyu G, Li S. Detection of liver and spleen stiffness in rats with portal hypertension by two-dimensional shear wave elastography. *BMC Med Imaging*. 2022;22(1):68. doi:10.1186/s12880-022-00786-6
40. Yang Y, Zhang JY, Ma ZJ, et al. Visualization of therapeutic intervention for acute liver injury using low-intensity pulsed ultrasound-responsive phase variant nanoparticles. *Biomater Sci*. 2024;12(5):1281–1293. doi:10.1039/D3BM01423A
41. Dai X, Du Z, Jin C, et al. Inulin-like polysaccharide ABWW may impede CCl(4) induced hepatic stellate cell activation through mediating the FAK/PI3K/AKT signaling pathway in vitro & in vivo. *Carbohydr Polym*. 2024;326:121637. doi:10.1016/j.carbpol.2023.121637
42. Xia Y, Luo Q, Gao Q, et al. SIRT1 activation ameliorates rhesus monkey liver fibrosis by inhibiting the TGF-β/smad signaling pathway. *Chem Biol Interact*. 2024;394:110979. doi:10.1016/j.cbi.2024.110979
43. Zhang C, Liu H, Cui Y, et al. Molecular magnetic resonance imaging of activated hepatic stellate cells with ultrasmall superparamagnetic iron oxide targeting integrin $\alpha v \beta_3$ for staging liver fibrosis in rat model. *Int J Nanomed*. 2016;11:1097–1108. doi:10.2147/IJN.S101366
44. Ullah A, Chen G, Hussain A, et al. Cyclam-modified polyethyleneimine for simultaneous TGFβ siRNA delivery and CXCR4 Inhibition for the treatment of CCl(4)-induced liver fibrosis. *Int J Nanomed*. 2021;16:4451–4470. doi:10.2147/IJN.S314367